applied sciences

MDPI

Article

Hydrodynamics and Musculature Actuation of Fish during a Fast Start

Yuhan Li [1,2], Jialei Song [2,*], Ling Yin [2], Bowen Jin [3], Bo Yin [4] and Yong Zhong [1,*]

[1] Shien-Ming Wu School of Intelligent Engineering, South China University of Technology, Guangzhou 511442, China
[2] School of Mechanical Engineering, Dongguan University of Technology, Dongguan 523808, China
[3] Beijing Computational Science Research Center, Beijing 100193, China
[4] Institute of Mechanics, Chinese Academy of Sciences, Beijing 100190, China
* Correspondence: songjl@dgut.edu.cn (J.S.); zhongyong@scut.edu.cn (Y.Z.)

Abstract: The fast start of fish is a rapid event that involves fast actuation in musculature and highly unsteady hydrodynamics. Fast-start capability is of great significance for fish to either hunt prey or escape from predators. In this study, we used a three-dimensional CFD model to study the hydrodynamics of a crucian carp during a C-type fast start. This study confirms the previous observations from both experiments and simulations that the jets are induced by the fast start for force generation, and the vortex rings generated in both the preparation and propulsion stages connect to each other. In addition, an obvious vortex ring generated by the head during the propulsion stage was observed, which potentially benefits the rotational motion during the fast start. According to the hydrodynamic information from CFD modeling, we established a model to analyze the internal torque, which represents the muscular actuation. The backward traveling speed of internal torque is 1.56 times the curvature speed, which confirms the existence of neuromechanical phase lag during the fast start of fish. This study potentially benefits the design of robot fish in terms of kinematics and driving mode.

Keywords: fast-start; fish swimming; musculature actuation; hydrodynamics

Citation: Li, Y.; Song, J.; Yin, L.; Jin, B.; Yin, B.; Zhong, Y. Hydrodynamics and Musculature Actuation of Fish during a Fast Start. *Appl. Sci.* **2023**, *13*, 2365. https://doi.org/10.3390/app13042365

Academic Editor: Roberto Camussi

Received: 10 January 2023
Revised: 3 February 2023
Accepted: 8 February 2023
Published: 12 February 2023

1. Introduction

The fast start of fish is a critical capability that significantly affects the consequences of hunting prey or escaping from predators [1]. The hydrodynamics of this process feature highly unsteady flows due to its short duration. For the teleost fish, the duration of a fast start is less than 30 ms, with maximum acceleration rates ranging from 22.7 to 39.5 ms^{-2} [2]. This short process is divided into three stages, shown in Figure 1: the preparation stage, the propulsion stage, and the completion stage [3]. According to the curvature of the middle line, the fast start of fish can be classified as a C-start or an S-start, with most predatory fish using S-start and herbivorous fish generally using C-start to escape [4,5].

The fast-start performance of larval fish has been studied, revealing the mechanism for achieving the stunning locomotive performance. Combining flow simulations and an evolutionary optimization algorithm, Gazzola et al. found that the traveling distance of a fast start is proportional to the bending curvature [6]. Li et al. reconstructed a larval model with high-fidelity geometry and kinematics and simulated the hydrodynamics. This work not only confirmed the finding of Gazzola et al., but also revealed that thrust is mainly produced in the posterior part of the body [7]. Following their study, Song et al. simulated the quick turning of larval fish, finding that the torque from the tail is the primary factor that contributes to the quick rotation [8]. Despite the difference in size, the flow around the larval and adult fish showed no qualitative differences [9]. As the flow around the adult fish is more dominated by inertial force, the fast-start movement of fish induces two types of forces: forces achieved by accelerating the adjacent fluid and lift forces contributing to

thrust by the fins [9,10]. Using digital particle imaging velocimetry (DPIV) technology, Tytell et al. measured the flow field evolution during the fast start of the bluegill sunfish [11]. The flow field was characterized by vortex pairs forming local jets that moved opposite to the body movement, which shows that the fast-start agility is directly related to the rapid generation of a vortex through body/tail flexing [12]. Using a geometric model and the kinematics of a fish body in the above experiment as input, the hydrodynamics during the fast-start process with three-dimensional numerical simulation showed details that could not be captured in the experiment: the wake structure of the fast start is a complex vortex structure composed of multiple vortex rings. Feng et al. [13] used numerical simulation to study the hydrodynamics of a virtual swimming C-turn of a tuna-like fish body. The pressure distribution on the swimmer's body surface showed that the thrust is mainly generated by the lunate tail. The vortex ring generated in the propulsion stage is elongated under the backflip of the tail, forming a wide and strong jet, which makes the fish slide forward quickly after the rotation.

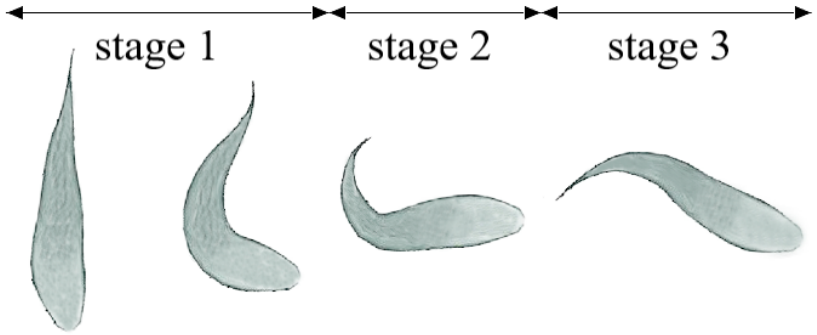

Figure 1. Illustration of the three stages of fish fast start. Stage 1, preparation stage: The middle line of the fish's body is bent from a straight line in the static state to a C or S shape, the center of mass (COM) of the fish's body is basically kept still, and the head turns toward the final direction of the fast start. Stage 2, propulsion stage: The tail swings in the opposite direction, the fish obtains the main forward thrust and starting acceleration, and its COM moves along a straight line or an arc. Stage 3, completion stage: The fish enters the cruising state through the small amplitude swing of the tail, or the fish keeps still and starts to slide, while the COM moves along a straight line.

Similar to cruising swimming, the fast start is powered by the muscles on both sides of the body. In cruising swimming, the torque signal or actuation of the muscle travels posteriorly, but faster than the bending wave of the body; this is called neuromechanical phase lag (NPL). In comparison, studies involving muscle activation and kinematics in the fast-start process show some differences. Although the backward-traveling wave exists during both the cruising and the fast start, the muscle strain during a fast start is much larger than that during cruising swimming and sprinting, resulting in a correspondingly larger torque [14,15]. During cruising swimming, only the red muscle of the fish is activated, but both the red and white muscles function simultaneously during a fast start. Ignoring the initial brief potentials, the muscles in the concave side are activated in stage 1 and are then followed by another high-amplitude Electromyography (EMG) on the contralateral side [16]. The EMG of the former has a larger amplitude, indicating the shortening effect is stronger than the lengthening [17]. In addition, the duration of EMG on the ipsilateral side increases along the body in stage 1, and the contralateral side remains the same but travels posteriorly [18,19], showing that the muscle activation in the fast-start process is transmitted backward and that the transmission speed is faster than that of the body bending wave, which implies NPL also exists during a fast start.

Although many studies have focused on the fast start of fish, muscle actuation during the fast start with detailed hydrodynamics has been less studied. In this paper, we obtained the hydrodynamics of fish fast starts through three-dimensional CFD, and then quantitatively analyzed the patterns of musculature activation using the internal torque.

2. Materials and Methods

2.1. Geometric Modeling and Kinematics

An adult *crucian* carp was used as the prototype for the fish model in our study (Figure 2a). The surface of the fish was reconstructed with triangular grids using the surface data from 3D scanning (ZGSCan 717, Guangzhou, China). To avoid numerical divergence in the fluid solver, the reconstructed surface was smoothed to remove the trivial details. The body trunk and tail of the carp were retained in the reconstructed model, while the other fins were trimmed out (Figure 2b). The fish body trunk is a three-dimensional block, and the caudal fin is a zero-thickness membrane structure. The entire fish mesh has 11,160 elements, including 9600 elements on the body surface and 1560 elements in the caudal fin. The length of the fish model was set as L = 1, the density is the same as the fluid $\rho = 1$, and the parameters of the model are shown in Table 1.

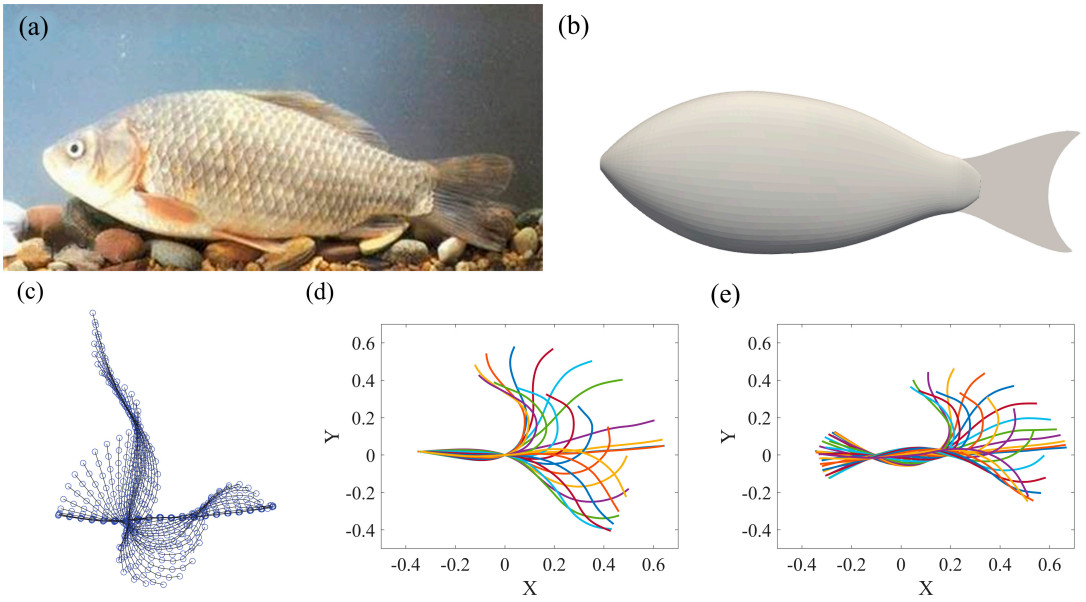

Figure 2. The reconstruction of the swimmer model and kinematics. (**a**) Fish prototype. (**b**) Fish model. (**c**) Midline extracted by Tytell et al. from video recordings of the bluegill sunfish escape process. (**d**) Keeping the front part horizontal and fixing the COM at the origin. (**e**) Midline kinematic inputs that satisfy conservation of linear momentum and angular momentum.

Table 1. Dimensionless parameters of the crucian carp model.

Parameter	Value
Mass	0.0192
Width	0.166
Height	0.3406
Area of tail	0.0382

The middle-line curves used in this paper were derived from video recordings of a bluegill sunfish escape process [11]. The kinematic curves were composed by extracting instantaneous coordinate values of 20 equidistant points along the fish middle line [20], as shown in Figure 2c. In our study, the rotation and propulsion of the fish originated from the reaction force of the fluid on the fish during the CFD solution, so we needed to know the kinematic curve of the fish when it is not acted upon by the fluid force as input. First, we adjusted the curve to ensure the conservation of linear and angular momentum. Conservation of linear momentum was achieved by fixing the COM at the origin; next, we assumed that the fish had an angular velocity $\omega_b(t)$ around the COM and calculated the angular momentum (Figure 2d). Conservation of angular momentum requires that

$dL_t/dt = 0$, so the angular velocity can be calculated; hence, the angle of rotation can be obtained as $\theta_b(t) = \int_0^t \omega_b(t)dt$. For each moment, we rotated the curve by $\theta_b(t)$ to ensure that the angular momentum was conserved. The method is described in detail in [21]. By the above method, we obtained middle-line kinematic input that satisfies the conservation of linear momentum and of angular momentum, as shown in Figure 2e.

2.2. Numerical Methods and Simulation Setup

The dynamics of three-dimensional incompressible, unsteady, viscous fluid around the swimmer was solved using a fluid solver based on the finite difference–immersed boundary method. The governing equations for the fluid around the swimmer are as follows:

$$\nabla \cdot \mathbf{u} = 0 \tag{1}$$

$$\frac{\partial \mathbf{u}}{\partial t} + (\mathbf{u} \cdot \nabla)\mathbf{u} = -\frac{1}{\rho}\nabla p + v\Delta \mathbf{u} \tag{2}$$

Here, $\mathbf{u}$ denotes the velocity vector, p denotes the pressure, and ρ and v are the density and kinematic viscosity of water, respectively. The equations were integrated in time using the fractional step method of van Kan [22]. A second-order Adams–Bashforth scheme was employed for the convective terms, while the diffusion terms were discretized using an implicit Crank–Nicolson scheme, which eliminates the viscous stability constraint. The Poisson equation for pressure updates was solved with a highly efficient geometric multigrid method that employs a line-based Gauss–Siedel successive-over-relaxation (SOR) smoother [23]. The fluid solver is able to simulate the motion of complex embedded objects, including zero-thickness membranes and three-dimensional solids, and has been successfully applied to the swimming of fish [8,24,25] and the flight of birds [26,27].

The entire flow field was discretized with a nonuniform Cartesian grid with dimensions of $8 \times 5.1 \times 5$ in the X, Y, and Z directions, using a total of $321 \times 341 \times 181 \approx 20$ million grid points. The grid was locally refined around the fish with a minimum spacing of $0.005 \times 0.005 \times 0.005$ (Figure 3b). We divided the whole fast-start process into 750 steps. The time interval for the simulation dt was set as 0.0013, so that the entire process had a period T = 0.975 and a characteristic velocity $U = L/T$ = 1.0256, where L = 1 is the characteristic length of the fish model. The Reynolds number is defined as $Re = UL/v$= 4102.4, where v= 1/4000 is the kinematic viscosity.

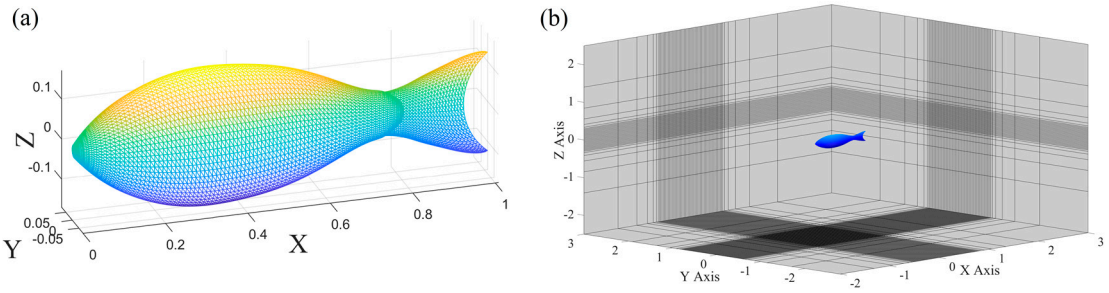

Figure 3. (**a**) Integrated fish model mesh with both the trunk and tail. (**b**) Nonuniform Cartesian mesh in the computational domain. Only one out of every five points in each direction is shown.

2.3. Internal Torque

With the data from the CFD simulation, we calculated the internal torque T along the fish body. The internal torque, or the torque exerted by the muscles on the intersection of the body, was calculated considering both the hydrodynamics and the body's inertia. The internal torque can be calculated on either side from the intersection of interest, as shown in Figure 4. In the figure, $\boldsymbol{f}$ denotes the specific fluid force on element dl, γ is its linear density along the fish middle line, $\boldsymbol{a}$ is the acceleration of the body segment, and $\mathbf{r}$ is the displacement from the intersection of interest.

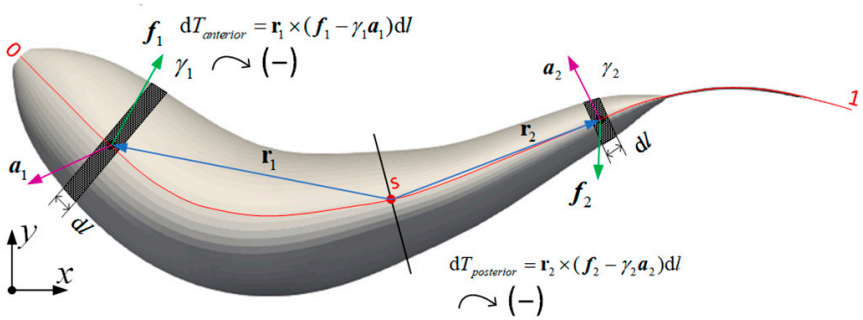

Figure 4. Diagram of internal torque. The black shaded area represents the element along the body axis.

Using d'Alembert's principle, the effective external force can be considered $\boldsymbol{f} - \gamma \boldsymbol{a}$. Then, the internal torque was calculated by integrating from the tail forward (Equation (3a)), or from the head backward (Equation (3b)).

$$T_{posterior}(s,t) = -\mathbf{e}_z \int_s^1 \mathbf{r} \times (\boldsymbol{f} - \gamma \boldsymbol{a}) dl \tag{3a}$$

$$T_{anterior}(s,t) = \mathbf{e}_z \int_0^s \mathbf{r} \times (\boldsymbol{f} - \gamma \boldsymbol{a}) dl \tag{3b}$$

Here, s is the arc length from the fish head and $\mathbf{e}_z$ denotes the unit vector in z direction. Theoretically, $T = T_{posterior} = T_{anterior}$; the relative error becomes apparent at the ends, where the torques are smaller. To reduce the error of the torque, the weighted average was used in the following formula:

$$T = sT_{posterior} + (1 - s)T_{anterior} \tag{4}$$

3. Results

3.1. Swimming Performance

Snapshots of the swimmer at four key moments are shown in Figure 5a. The color on the surface presents the velocity magnitude distribution. Because the body of the swimmer is deforming, the governing equation for the angular degree of freedom is $d(I\omega)/dt = T_{tot}$, where I is the moment of inertia, ω is the angular velocity of the body, and T_{tot} is the total torque computed by integrating the contributions from the hydrodynamic forces on the surface of the swimmer. Since the deformation is prescribed, I and $\dot{I}$ are known parameters. The angular velocity of the whole fish ω can be obtained by numerically solving equation $\dot{\omega} = (T_{tot} - \dot{I}\omega)/I$, and subsequently, the angle is obtained.

Figure 5b shows the temporal variation of the swimmer's heading angle and angular velocity during a fast start. It can be seen in the figure that at t/T = 0.43, the heading angle reaches the maximum value of 1.34 rad. After that, the angular velocity changes direction, and the heading angle gradually decreases until t/T = 0.76, and the angular velocity direction changes again. At this time, the heading angle is 0.52 rad. The change in the angle and angular velocity is consistent with the definitions of stage 1 and stage 2 in [11]; that is, stage 1 is the period from the beginning of movement to the change in the angular velocity (here we ignore the sign change in angular velocity in the short time after the beginning of movement), and stage 2 is the period from the end of stage 1 to the change in the angular velocity again. Figure 5c shows the trajectory of the swimmer's COM. It can be seen that in stage 1, the COM covers a small distance to the left and down as the body bends into a C-shape. At the beginning of stage 2, the displacement direction turns to the escape direction and moves quickly. At stage 3, the swimmer continues to swim forward. The transitional velocity time course during the rotation process is shown in Figure 5d. An

interesting feature is that the speed increases significantly in stage 2, indicating a large net propulsion force.

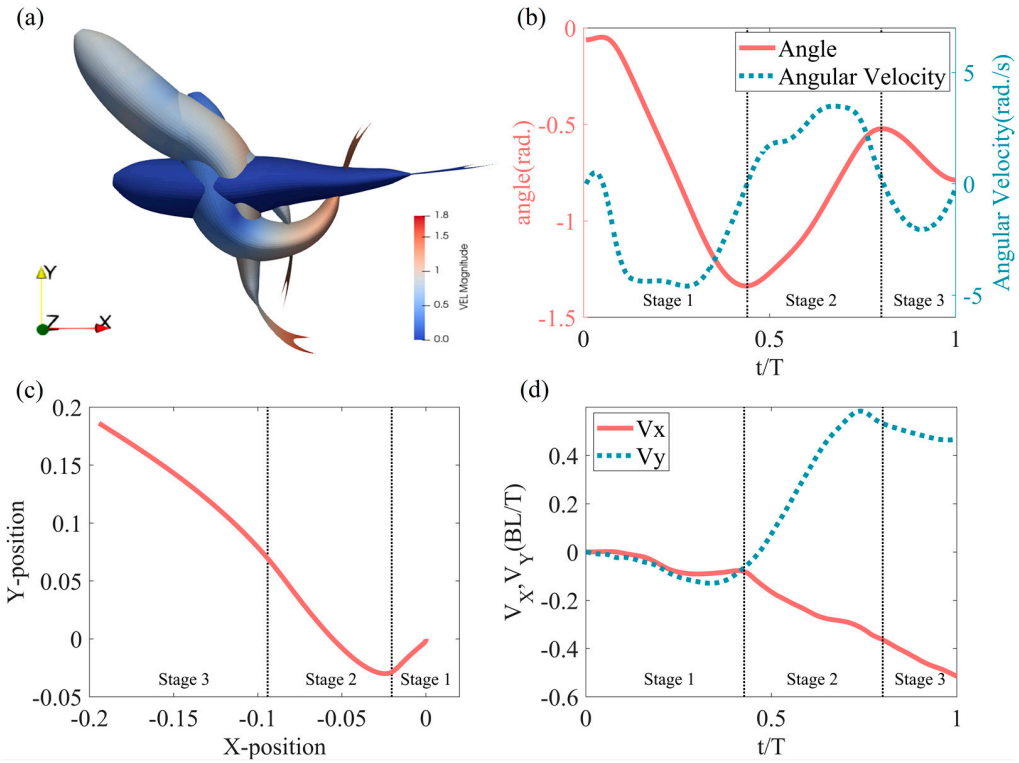

Figure 5. (**a**) Snapshots of the fish at t/T = 0, 0.43 (end of stage 1), 0.76 (end of stage 2), and 1. (**b**) The time course of heading angle and angular velocity. (**c**) Translational motion. (**d**) Translational velocity. The black dotted line is the stage separation line.

3.2. Force, Torque, and Power

The force components, F_X,F_Y, and F_Z, are normalized by the fluid density ρ, the maximum cross-sectional area $S = 0.044L^2$, and the characteristic velocity U. Thus, the normalized forces are as follows:

$$C_X = \frac{F_X}{0.5\rho U^2 S}, \; C_Y = \frac{F_Y}{0.5\rho U^2 S}, \; C_Z = \frac{F_Z}{0.5\rho U^2 S} \tag{5}$$

Since the geometry of the fish model is vertically symmetrical, the vertical force distribution cancels out, resulting in zero values for C_Z and F_Z of the entire swimmer. To analyze the role of the body and tail in the fast-start process, we show the temporal variation of the force coefficient on the whole swimmer, the body trunk, and the tail, as shown in Figure 6. The temporal variation of the force coefficient in the X direction shows several remarkable features. First, the signs of C_X on the body and tail are almost always opposite. The force on the body causes drag, while the tail contributes the thrust. Second, the force coefficient changes gently in stage 1, while it changes steeply in stage 2, with two peaks and troughs. The swimmer's total force coefficient curve is very close to the tail force coefficient curve, sharing the similar variation trend and amplitude. This means that the tail plays a major role in the force and motion in the Y direction. For torque, because the arm of the lateral force on the tail fin is large, the characteristics of the torque change process are similar to the lateral force, as shown in Figure 6c.

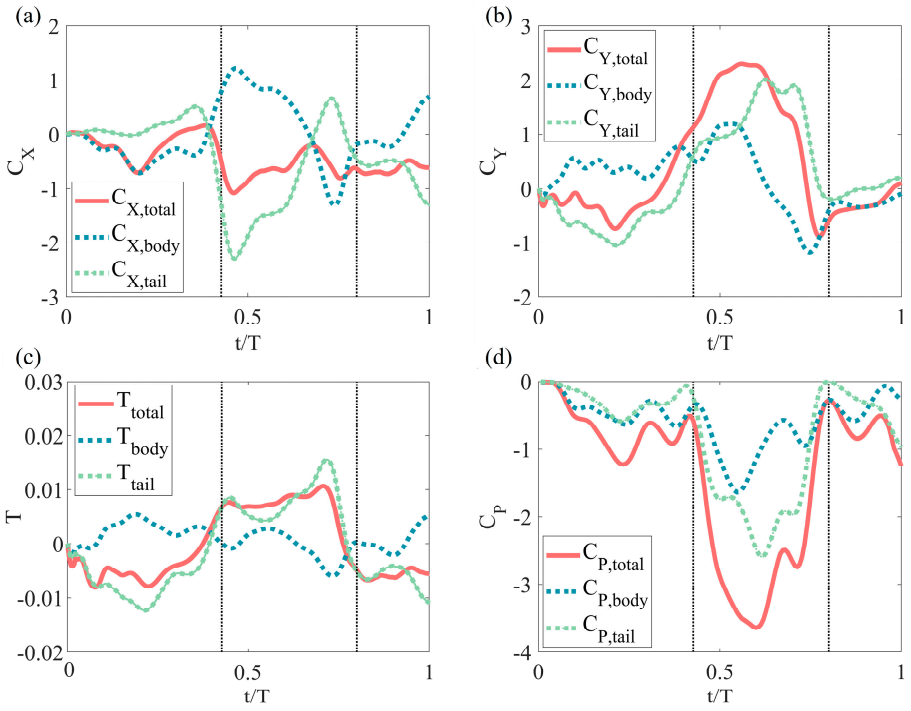

Figure 6. Hydrodynamic parameters of the fast start. Force coefficient in X (**a**) and Y (**b**) directions and torque (**c**) and hydrodynamic power output (**d**) of the entire body, the body trunk, and the tail.

The hydrodynamic power is calculated by the integration on the swimmer model surface of the dot product of the force and velocity: $P = \int_\Omega \mathbf{f} \cdot \mathbf{u} dS$. Moreover, the power coefficient is defined as $C_P = P/(0.5\rho U^3 S)$. The temporal variation in power coefficients is shown in Figure 6d. A negative power coefficient throughout the entire process indicates the swimmer's work on the fluid, and little energy is recaptured by the swimmer. Compared with that of stages 1 and 3, the power coefficient of the second stage is much larger. In addition, it is worth noting that at the time of switching between the first and second stages, as well as between the second and third stages, the power coefficient decreases significantly. This is because the direction of the swimmer's swing changes during stage switching, thus making use of the jet generated in the previous stage. The fluid works on the swimmer, reducing the latter's output power.

3.3. Flow Field

To explore the interaction of the swimmer and the surrounding flow field in a fast start, we analyzed the velocity vector and vorticity ω_Z of the flow field near the swimmer. Figure 7 shows four typical instantaneous snapshots for specific analysis. In Figure 7a, the fluid near the swimmer starts to flow under the swimmer's deformation, and two initial vortices are formed near the head and tail. Figure 7b shows a snapshot of the flow field at the moment of switching from stage 1 to stage 2. As the body bends into a C-shape, three jets and two clockwise vortices are formed near the head, waist, and tail. After that, the swimmer enters stage 2 and starts to swing its body in reverse. The head will receive the hydrodynamic force in jet 3, and the tail will receive the hydrodynamic force in jet 1. At the time instant of switching between stage 2 and stage 3, the principle of fluid doing work to the swimmer is similar, which further explains the reason why the swimmer's output power is significantly reduced during stage switching. Figure 7c shows a snapshot of the flow field at the moment of stage 2 and stage 3 switching. Because the swing speed of stage 2 is faster than that of stage 1, the three jets develop more strongly, and three anti-clockwise vortexes, VT4, VT5, and VT6, successively appear at the interface of jet 1 and jet 2, which is similar to the results in [28]. In addition, the vortex induced by the head is clearly captured. In stage 1, the rapid rotation of the anterior part generates a vortex

(VT2 in Figure 7b) and induces the flow to move inward to the head (jet 3 in Figure 7b). This VT2 causes the drag and torque that obtrudes the clockwise rotation of the fish. However, in stage 2, the head causes the vortex on the other side (VT2 and VT3 in Figure 7c), and this vortex moves backward along the body (Figure 7d).

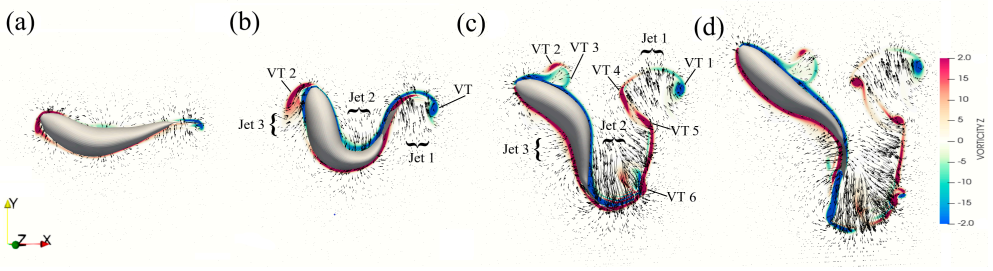

Figure 7. Four snapshots of the flow in the mid-plane visualized by velocity vectors and vorticity ω_Z. (**a**) t/T = 0.17. (**b**) t/T = 0.43, the moment of the end of stage 1. (**c**) t/T = 0.76, the moment of the end of stage 2. (**d**) t/T = 1, the last moment of the fast start.

Figure 8 shows the 3D wake structure of the flow field around the swimmer at four instants corresponding to the in-plane flow shown in Figure 7. From a 3D perspective, the tail or the posterior part generates a vortex ring in stage 1 (R1), within which a strong jet 1 is generated (Figure 7b). Meanwhile, obvious leading-edge vortices on the top and bottom of both the anterior body and the part before the peduncle are formed (Figure 8b). In stage 2, the clockwise rotation of the head induces a vortex ring (Figure 8c), corresponding to VT2 and VT3 in Figure 7c. Then, it is shed backward along the fish body. More obviously, another large vortex ring (R2) is generated on the tail, connecting to the vortex ring formed in stage 1. Within R2, a strong jet 2 is induced, resulting in a large thrust. The flow of this jet 2 originates from jet 2, as shown in Figure 8b, which implies that the vortex ring R2 might be affected by the preparation stage.

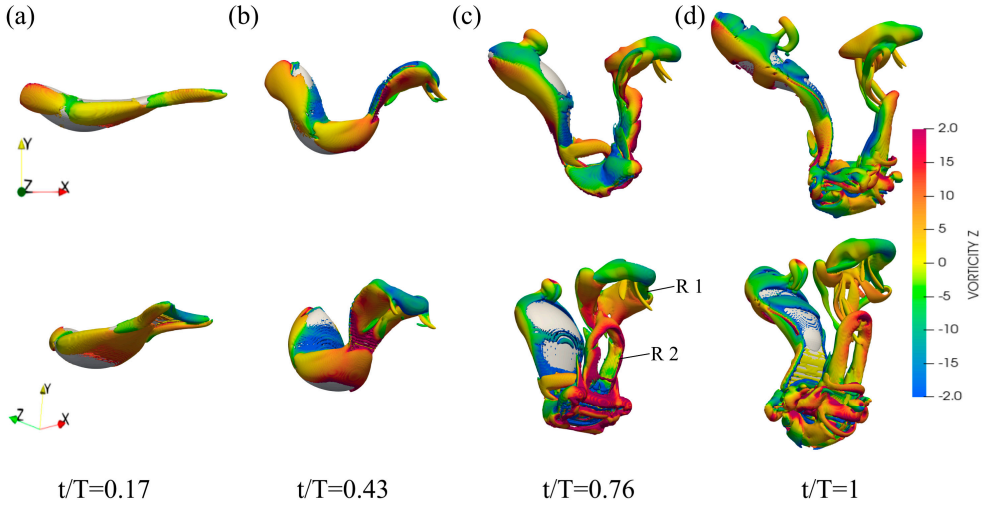

Figure 8. Three-dimensional vortex structures in the flow at four moments of different perspective. (**a**) t/T = 0.17. (**b**) t/T = 0.43, the moment of the end of stage 1. (**c**) t/T = 0.76, the moment of the end of stage 2. (**d**) t/T = 1, the last moment of the fast start.

3.4. Internal Torque

The spatiotemporal distribution of the internal torque to overcome the inertia force and hydrodynamic force is shown in Figure 9a. It can be seen in the figure that the internal torque is mainly distributed in the middle position 0.18L < s < 0.81L, defined by 30% of the maximum value, which means that the main power driving the body to swing in the fast start is the contraction of the muscle in the middle position. The positive and negative

values indicate that the muscles on different sides are activated, as the muscle is assumed to be merely able to generate tension. Although muscle activity is also observed on the convex side, its intensity is significantly weaker than that on the bending side [17,18].The black solid line and dotted line in Figure 9a show the spatiotemporal distribution of the maximum and minimum curvature in the internal torque concentration area. The curvature of the initial bending side is positive, and the curvature of the convex bending side is negative. Both the maximum curvature and minimum curvature show an obvious backward propagation trend, and the backward propagation speed (BL/T) of the maximum curvature in stage 1, ν_κ = 1.005, is smaller than that of the minimum curvature in stage 2, ν_κ = 1.571. This speed is less than that of the muscle activation, showing the NPL during a fast start. Figure 9b shows the temporal variation of the internal torque at the middle of the fish (s/L = 0.5) and at the peduncle (s/L = 0.76). In addition to the difference in magnitude of these two internal torques, the phase is also different, with the torque having a more advanced phase. The internal torque on the middle body shows a sharp variation between stage 1 and stage 2, and the rapid change in both magnitude and sign indicates the coordination of the muscles on both sides. The torque on the peduncle mainly refers to the torque due to the structure elasticity or viscosity, as the muscle volume is small. In this paper, we do not distinguish this, as the muscles dominate the internal torque. Figure 9c shows the internal torque or muscle activation during the fast start, with the black area indicating the portion where the muscle is activated. It can be seen from the figure that the direction of the internal torque symbol has changed before the end of stage 1 and stage 2, which means that the muscles on the bending side of stage 2 and stage 3 do not start to activate from this stage, but start before the end of the previous stage, which is consistent with the explanation of [29].

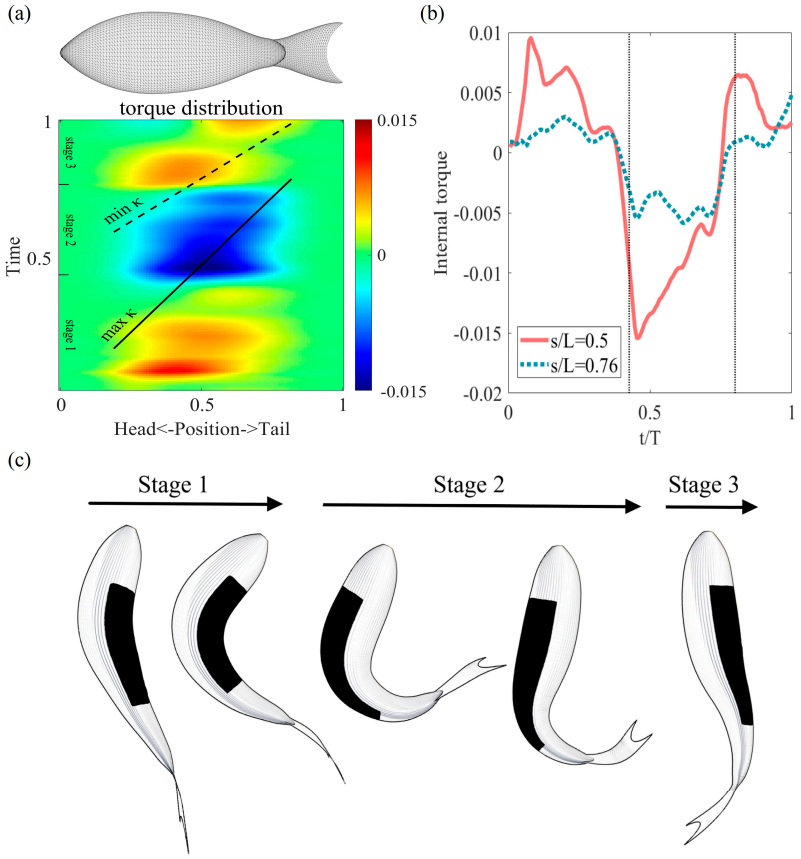

Figure 9. (**a**) Spatiotemporal distribution of the internal torque. The solid and dashed lines indicate the maximum and minimum curvatures, respectively. (**b**) The torque variation with time on middle body (s/L = 0.5) and peduncle (s/L = 0.76). (**c**) Schematic of muscle actuation.

4. Discussion

4.1. Roles of the Other Fins

As observed by researchers, the median fins are usually fully erected prior to acceleration or soon after the beginning of acceleration [30,31]. Meanwhile, the paired fins are abducted and pressed against the body during the quick start [5,10]. In our simulation, only the caudal fin was included in the model, and the absence of the dorsal fin and anal fin might cause some error in the rotation of the fish. Borazjani et al. used an integrated sunfish model to study a C-start. The vortex induced by the dorsal fin indicates that at both the preparation and propulsion stages, the dorsal fin generates a negligible amount of force that contributes to the transitional and rotational motion [20]. As the dorsal fin of the model in their paper is located on the rear part of the trunk, the lateral forces on it could generate sufficient torque for rotation; for the fish with dorsal fins located right above the middle trunk, when the fin is erected to increase the surface area, the starting translational movement would be enhanced in the direction on the convex side. However, such enhancement is trivial compared to the overall translational movement during the quick start (0.035 BL versus 0.261 BL in our study), indicating that the dorsal fin might not contribute much to the transnational movement, but might benefits the rotation during quick swimming. This argument is supported by Webb's study, which stated that his data were too variable to formulate conclusions on the effects of median fin amputation and he could not detect a significant effect of the dorsal and anal fins, despite the theory suggesting that the increase in depth of the fish (by fins) should increase the C-start performance [10].

4.2. Effects of the Reynolds Number

In our study, the Reynolds number is approximately 4000, which is much smaller than that of real adult fish. Borazjani et al. studied the effect of the Reynolds number using both viscous and inviscid simulations. They showed that the inviscid simulation provides a much more complex 3-D vortex structure, but the key features of the flow are the same during the entire fast start [28]. As a Reynolds number of ~4000 is in the regime where the inertial forces dominate the viscous force, our study is able to present the case of a real fish fast start. To further validate our argument of Re effects, we simulated the same kinematics at Re~8000 and 12,000. At different Re, both the movement of the COM and the rotation angles are slightly changed (0.261 BL versus 0.290 BL versus 0.296 BL on the COM, and 0.72 rad versus 0.74 rad versus 0.75 rad). However, although the vortex structures at Re~8000 and 12,000 are more fractured, the overall structures are quite similar (Video S1–S3), showing that the mechanism we are investigating is the same.

5. Conclusions

In this study, we used three-dimensional CFD modeling to study the hydrodynamics of a crucian carp during a C-type fast start. The study confirms the previous observations from both experiments and simulations of the jets that are induced by the fast start for force generation and the connecting vortex rings that produced in the preparation and propulsion stage separately. In addition, an obvious vortex ring generated by the head during the propulsion stage was observed, which potentially benefits the rotational motion during the fast start. According to the hydrodynamic information from the CFD modeling, we established a model to analyze the internal torque, which represents the muscle actuation. The backward traveling speed of the internal torque is 1.56 times that of the curvature speed, which confirms the existence of a neuromechanical phase lag during the fast start of fish. The internal torque to overcome the inertial and hydrodynamic torques indicates the activation model of the muscles on both sides of the fish during the movement, and compares its distribution with the change process of the middle line curvature. It was found that the bending of the fish body is transmitted backward and lags behind the activation of the muscle at the bending side.

Supplementary Materials: The following supporting information can be downloaded at: https://www.mdpi.com/article/10.3390/app13042365/s1, Video S1: Vortex structure at Reynolds number of 4000; Video S2: Vortex structure at Reynolds number of 8000; Video S3: Vortex structure at Reynolds number of 12000.

Author Contributions: Conceptualization, L.Y. and Y.Z.; Methodology, J.S. and B.J.; Software, Y.L., J.S. and B.J.; Formal analysis, Y.L.; Investigation, Y.L.; Resources, L.Y., B.Y. and Y.Z.; Data curation, Y.L.; Writing – original draft, Y.L.; Writing – review & editing, J.S., L.Y. and Y.Z.; Supervision, J.S. and Y.Z.; Funding acquisition, J.S. and Y.Z. All authors have read and agreed to the published version of the manuscript.

Funding: This work is supported by the Guangdong Basic and Applied Basic Research Foundation (No. 2020A1515110584) and the DGUT startup grant (No. 211135014) to JS, the Guangdong Provincial Key Laboratory of Intelligent Disaster Prevention and Emergency Technologies for Urban Lifeline Engineering (No.2022B1212010016) to LY and JS, and the Natural Science Foundation of Guangdong Province (No. 2022A1515011479) and the National Natural Science Foundation of China under grant (No. 62103152) to YZ.

Institutional Review Board Statement: Not applicable.

Informed Consent Statement: Not applicable.

Data Availability Statement: All data files are available from the GitHub database: https://github.com/songjialei/fishquickstart.git.

Conflicts of Interest: The authors declare no conflict of interest.

References

1. Fish, F.; Lauder, G.V. Passive and active flow control by swimming fishes and mammals. *Annu. Rev. Fluid Mech.* **2006**, *38*, 193–224. [CrossRef]
2. Budick, S.A.; O'Malley, D.M. Locomotor repertoire of the larval zebrafish: Swimming, turning and prey capture. *J. Exp. Biol.* **2000**, *203*, 2565–2579. [CrossRef]
3. Wakeling, J. Biomechanics of fast-start swimming in fish. *Comp. Biochem. Physiol. Part A Mol. Integr. Physiol.* **2001**, *131*, 31–40. [CrossRef]
4. Domenici, P.; Blake, R. The kinematics and performance of fish fast-start swimming. *J. Exp. Biol.* **1997**, *200*, 1165–1178. [CrossRef] [PubMed]
5. Webb, P. Fast-start performance and body form in seven species of teleost fish. *J. Exp. Biol.* **1978**, *74*, 211–226. [CrossRef]
6. Gazzola, M.; Van Rees, W.M.; Koumoutsakos, P. C-start: Optimal start of larval fish. *J. Fluid Mech.* **2012**, *698*, 5–18. [CrossRef]
7. Li, G.; Müller, U.K.; van Leeuwen, J.L.; Liu, H. Body dynamics and hydrodynamics of swimming fish larvae: A computational study. *J. Exp. Biol.* **2012**, *215*, 4015–4033. [CrossRef] [PubMed]
8. Song, J.; Zhong, Y.; Luo, H.; Ding, Y.; Du, R. Hydrodynamics of larval fish quick turning: A computational study. *Proc. Inst. Mech. Eng. Part C J. Mech. Eng. Sci.* **2018**, *232*, 2515–2523. [CrossRef]
9. Weihs, D. A hydrodynamical analysis of fish turning manoeuvres. *Proc. R. Soc. London. Ser. B Biol. Sci.* **1972**, *182*, 59–72.
10. Weihs, D. The mechanism of rapid starting of slender fish. *Biorheology* **1973**, *10*, 343–350. [CrossRef] [PubMed]
11. Tytell, E.D.; Lauder, G.V. Hydrodynamics of the escape response in bluegill sunfish, Lepomis macrochirus. *J. Exp. Biol.* **2008**, *211*, 3359–3369. [CrossRef] [PubMed]
12. Triantafyllou, M.S.; Triantafyllou, G.; Yue, D. Hydrodynamics of fishlike swimming. *Annu. Rev. Fluid Mech.* **2000**, *32*, 33–53. [CrossRef]
13. Feng, Y.; Liu, H.; Su, Y.; Su, Y. Numerical study on the hydrodynamics of C-turn maneuvering of a tuna-like fish body under self-propulsion. *J. Fluids Struct.* **2020**, *94*, 102954. [CrossRef]
14. Ellerby, D.; Altringham, J. Spatial variation in fast muscle function of the rainbow trout Oncorhynchus mykiss during fast-starts and sprinting. *J. Exp. Biol.* **2001**, *204*, 2239–2250. [CrossRef]
15. Wakeling, J.M.; Johnston, I.A. Muscle power output limits fast-start performance in fish. *J. Exp. Biol.* **1998**, *201*, 1505–1526. [CrossRef] [PubMed]
16. Jayne, B.; Lauder, G. Red and white muscle activity and kinematics of the escape response of the bluegill sunfish during swimming. *J. Comp. Physiol. A* **1993**, *173*, 495–508. [CrossRef]
17. Westneat, M.W.; Hale, M.E.; McHenry, M.J.; Long, J.H. Mechanics of the fast-start: Muscle function and the role of intramuscular pressure in the escape behavior of Amia calva and Polypterus palmas. *J. Exp. Biol.* **1998**, *201*, 3041–3055. [CrossRef]
18. Tytell, E.D.; Lauder, G.V. The C-start escape response of Polypterus senegalus: Bilateral muscle activity and variation during stage 1 and 2. *J. Exp. Biol.* **2002**, *205*, 2591–2603. [CrossRef]

19. Wakeling, J.M.; Johnston, I.A. Predicting muscle force generation during fast-starts for the common carp Cyprinus carpio. *J. Comp. Physiol. B* **1999**, *169*, 391–401. [CrossRef]
20. Borazjani, I. The functional role of caudal and anal/dorsal fins during the C-start of a bluegill sunfish. *J. Exp. Biol.* **2013**, *216*, 1658–1669. [CrossRef]
21. Ming, T.; Jin, B.; Song, J.; Luo, H.; Du, R.; Ding, Y. 3D computational models explain muscle activation patterns and energetic functions of internal structures in fish swimming. *PLoS Comput. Biol.* **2019**, *15*, e1006883. [CrossRef] [PubMed]
22. van Kan, J. A second-order accurate pressure-correction scheme for viscous incompressible flow. *SIAM J. Sci. Stat. Comput.* **1986**, *7*, 870–891. [CrossRef]
23. Dong, H.; Mittal, R.; Najjar, F. Wake topology and hydrodynamic performance of low-aspect-ratio flapping foils. *J. Fluid Mech.* **2006**, *566*, 309–343. [CrossRef]
24. Song, J.; Zhong, Y.; Du, R.; Yin, L.; Ding, Y. Tail shapes lead to different propulsive mechanisms in the body/caudal fin undulation of fish. *Proc. Inst. Mech. Eng. Part C J. Mech. Eng. Sci.* **2021**, *235*, 351–364. [CrossRef]
25. Zhong, Y.; Wu, J.; Wang, C.; Li, Y.; Song, J. Hydrodynamic effects of the caudal fin shape of fish in carangiform undulatory swimming. *Proc. Inst. Mech. Eng. Part C: J. Mech. Eng. Sci.* **2022**, *236*, 6385–6394. [CrossRef]
26. Song, J.; Luo, H.; Hedrick, T.L. Three-dimensional flow and lift characteristics of a hovering ruby-throated hummingbird. *J. R. Soc. Interface* **2014**, *11*, 20140541. [CrossRef]
27. Song, J.; Tobalske, B.W.; Powers, D.R.; Hedrick, T.L.; Luo, H. Three-dimensional simulation for fast forward flight of a calliope hummingbird. *R. Soc. Open Sci.* **2016**, *3*, 160230. [CrossRef]
28. Borazjani, I.; Sotiropoulos, F.; Tytell, E.D.; Lauder, G.V. Hydrodynamics of the bluegill sunfish C-start escape response: Three-dimensional simulations and comparison with experimental data. *J. Exp. Biol.* **2012**, *215*, 671–684. [CrossRef]
29. Goldbogen, J.A.; Shadwick, R.E.; Fudge, D.S.; Gosline, J.M. Fast-start muscle dynamics in the rainbow trout Oncorhynchus mykiss: Phase relationship of white muscle shortening and body curvature. *J. Exp. Biol.* **2005**, *208*, 929–938. [CrossRef]
30. Eaton, R.C.; Bombardieri, R.A.; Meyer, D.L. The Mauthner-initiated startle response in teleost fish. *J. Exp. Biol.* **1977**, *66*, 65–81. [CrossRef]
31. Webb, P. Effects of median-fin amputation on fast-start performance of rainbow trout (*Salmo gairdneri*). *J. Exp. Biol.* **1977**, *68*, 123–135. [CrossRef]